nature methods

ARTICLES

https://doi.org/10.1038/s41592-019-0326-x

Corrected: Publisher Correction

Noninvasive monitoring of single-cell mechanics by acoustic scattering

Joon Ho Kang[1,2], Teemu P. Miettinen[1,3], Lynna Chen[4], Selim Olcum[1], Georgios Katsikis[1], Patrick S. Doyle[1,5] and Scott R. Manalis[1,4,6*]

The monitoring of mechanics in a single cell throughout the cell cycle has been hampered by the invasiveness of mechanical measurements. Here we quantify mechanical properties via acoustic scattering of waves from a cell inside a fluid-filled vibrating cantilever with a temporal resolution of < 1 min. Through simulations, experiments with hydrogels and the use of chemically perturbed cells, we show that our readout, the size-normalized acoustic scattering (SNACS), measures stiffness. To demonstrate the noninvasiveness of SNACS over successive cell cycles, we used measurements that resulted in deformations of < 15 nm. The cells maintained constant SNACS throughout interphase but showed dynamic changes during mitosis. Our work provides a basis for understanding how growing cells maintain mechanical integrity, and demonstrates that acoustic scattering can be used to noninvasively probe subtle and transient dynamics.

Although spatiotemporal changes in cytoskeletal components have been widely characterized by optical microscopy[1,2], mechanical measurements are necessary for a full understanding of the functional consequences of cytoskeletal remodeling[3]. Mechanical properties of living cells such as stiffness often play a fundamental role in various intra- and intercellular processes such as migration[4], metastasis[5,6] and development[7]. Numerous strategies have been introduced for measuring mechanical properties of single cells, from atomic force microscopy (AFM)[8,9] to optical stretching[10–12], fluid shear stress[13,14] and particle-tracking methods[15–17], but they are typically invasive and used as end-point assays. Changes in stiffness can be continuously monitored by means of microindentation and AFM techniques involving a series of indentations across the top surface of a cell[18,19]. However, these measurements are influenced by the geometry of the indenter tip and the location of its physical contact, which makes long-term monitoring of whole-cell stiffness with high temporal resolution challenging. Recently, acoustic fields have been used to noninvasively probe cellular stiffness[20–22]. This is typically achieved via the application of acoustic radiation forces in microchannels and tracking of the stiffness-dependent trajectories of cells to obtain end-point measurements.

Here we introduce an acoustic method for continuous and noninvasive monitoring of single-cell mechanics over multiple cell generations. This approach enabled us to precisely follow the mechanical dynamics of single cells in time scales of less than 1 min and observe mechanical changes too subtle to be observed at the population level because of cellular heterogeneity.

Results

Acoustic scattering shifts resonant frequency at the node of a suspended microchannel resonator. We used the vibration of a suspended microchannel resonator (SMR; Fig. 1a, top) as an acoustic energy source and investigated whether the scattered acoustic fields from the cell provided a signal that we could use to monitor its mechanical properties (Fig. 1b). The SMR is a cantilever-based microfluidic mass sensor that has previously been used to measure cell buoyant mass[23]. Vibration of the SMR at its second mode (resonant frequency f) causes the vibration amplitude to vary along the length of the cantilever, with one local maximum (antinode) near the center and a zero-minimum (node) near the tip (Fig. 1a, middle). When a cell is at the antinode, the net change in mass (i.e., the buoyant mass of the cell) corresponds to a change in the kinetic energy of the system[24], and thus causes a shift in the resonant frequency of the SMR ($\Delta f/f|_{\mathrm{antinode}}$) (Fig. 1a, bottom, and Supplementary Note 1). When the cell is at the node, the net change in mass is not expected to shift the resonant frequency ($\Delta f/f|_{\mathrm{node}} = 0$) because the vibration amplitude is zero and there is no change in kinetic energy. However, we observed a consistent resonant frequency shift at the node ($\Delta f/f|_{\mathrm{node}} \neq 0$) when we flowed a single cell or polystyrene bead in the SMR (Fig. 1a, bottom). This resonant frequency shift, which we termed node deviation ($\Delta f/f|_{\mathrm{node}}$), was different for cells and beads of similar buoyant mass. We therefore hypothesized that the node deviation corresponds to an energy change due to acoustic scattering from the cell's surface, and that the node deviation depends on cellular mechanical properties.

First, to determine whether node deviation corresponds to acoustic scattering, we used finite element method (FEM) simulations for fluid–structure acoustic interactions (Supplementary Note 2). This revealed that the acoustic pressures and velocities varied along the SMR, similarly to the vibration amplitude (Fig. 1c, Supplementary Fig. 1 and Supplementary Video 1). Positioning a particle at the node changed the acoustic velocities (Fig. 1c, inset, and Supplementary Video 2). When we calculated the resonant frequency shift by integrating the acoustic energy terms obtained from the simulation (Supplementary Tables 1 and 2 and Supplementary Note 2), we obtained excellent agreement ($R^2 = 0.984$) with our measurements (Fig. 1d). We confirmed that the particle–fluid density difference had a negligible effect on node deviation (Supplementary Fig. 2).

[1]Koch Institute for Integrative Cancer Research, Massachusetts Institute of Technology, Cambridge, MA, USA. [2]Department of Physics, Massachusetts Institute of Technology, Cambridge, MA, USA. [3]MRC Laboratory for Molecular Cell Biology, University College London, London, UK. [4]Department of Biological Engineering, Massachusetts Institute of Technology, Cambridge, MA, USA. [5]Department of Chemical Engineering, Massachusetts Institute of Technology, Cambridge, MA, USA. [6]Department of Mechanical Engineering, Massachusetts Institute of Technology, Cambridge, MA, USA.
*e-mail: srm@mit.edu

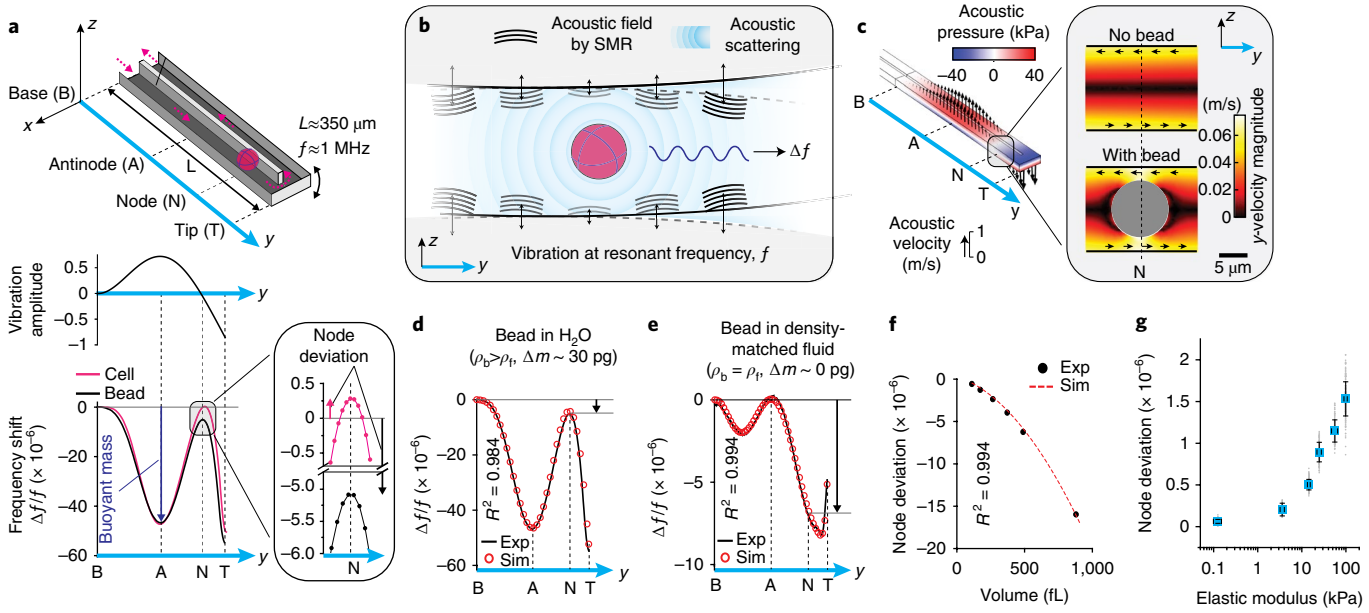

Fig. 1 | Acoustic scattering causes a resonant frequency shift at the node of an SMR. a, Top, schematic of the SMR with a particle flowing through the embedded fluidic channel. Pink arrows mark the particle trajectory. Middle, normalized vibration amplitude at the second mode. Bottom, the resonant frequency shift ($\Delta f/f$) from experiments with a single cell (pink) and a polystyrene bead (black). Vertical dashed lines mark the particle positions along the cantilever, as in the schematic at the top. Buoyant mass (size) is measured at the antinode ($\Delta f/f|_{\text{antinode}}$; blue arrow). The zoomed-in plots on the right highlight $\Delta f/f$ at the node where node deviation was measured ($\Delta f/f|_{\text{node}}$; black and pink arrows). **b**, A conceptual illustration of frequency shift due to acoustic scattering. A particle interacts with acoustic fields (black waves) generated by the SMR vibration (black arrows) at resonant frequency f. The particle–fluid interaction causes acoustic scattering (blue waves), which shifts the resonant frequency (Δf). The wavelength (λ) of the acoustic fields is depicted qualitatively (λ ~ 1 mm, which is ~100 times the channel height). **c**, Acoustic pressure (color-coded according to the key) and acoustic velocities (arrows) in the SMR from FEM simulations. The zoomed-in schematic on the right shows magnitudes of y-acoustic velocities with and without a polystyrene bead at the node. Black arrows indicate the directions of y-acoustic velocities. **d**,**e**, $\Delta f/f$ from simulations (Sim; red circles) and experiments (Exp; black lines) with polystyrene beads flowing through an SMR filled with (**d**) H_2O or (**e**) density-matched fluid. Black arrows show node deviation. ρ_b, ρ_{bead}; ρ_f, ρ_{fluid}. **f**, Node deviation versus particle volume from simulations (red dashed line) and experiments (black dots) with polystyrene beads. **g**, Node deviation versus mean elastic modulus, as measured via AFM indentation (Methods), for synthetic hydrogels of same volume (n = 92, 115, 243, 146, 134 and 186 hydrogels for node deviation measurements; n = 4 hydrogels for each AFM measurement). Data depict mean (blue squares) ± s.d. (error bars).

To validate that acoustic effects can be measured independently of buoyant mass, we measured a bead in a density-matched fluid ($\rho_{\text{fluid}} = \rho_{\text{bead}}$). This resulted in zero resonant frequency shift at the antinode ($\Delta f/f|_{\text{antinode}} = 0$) but a noticeable resonant frequency shift at the node in both the experiment and the simulation, which showed excellent agreement with each other ($R^2 = 0.994$; Fig. 1e). Additional measurements revealed that node deviation was independent of fluid velocity and vibration amplitude (Supplementary Fig. 3a,b). Therefore, by measuring the resonant frequency shift at the node and antinode as cells flow through the SMR, one can simultaneously and independently quantify the acoustic scattering and buoyant mass of a cell (Fig. 1a, bottom).

We compared polystyrene particles with different volumes and observed that node deviation changed with particle volume (Fig. 1f). The volume dependence could be accounted for by the buoyant mass measurement. To establish the correlation between node deviation and stiffness, we fabricated hydrogels with varying elastic modulus by changing their chemical composition, and characterized the elastic modulus of the hydrogels by AFM. When measuring the mechanical properties with the SMR, we observed that the node deviation of the hydrogels increased monotonically with their elastic modulus over the range of 0.1–100 kPa (Fig. 1g). We also observed that node deviation was not sensitive to particle shape for hydrogels of the same elastic modulus and aspect ratios in the range of 1–2.5 (Supplementary Fig. 3c).

Size-normalized acoustic scattering depends on cell cortex mechanical properties. Next, we asked whether mechanical properties of live cells could be probed through measurement of the node deviation. We implemented the 'cortical shell–liquid core' model[25] in our FEM simulation (Fig. 2a), which highlights the role of actomyosin cortex in cell mechanics[26,27]. We calculated that the acoustic interactions caused relatively small deformations (< 15 nm) on the cell surface (Supplementary Note 2), which suggested that node deviation may be governed primarily by the actomyosin cortex[28]. We then compared our FEM simulations with the node deviation of mouse lymphoblast (L1210) cells (Fig. 2b). The FEM simulations yielded similar range signals as the experiments when we used an elastic modulus of 4–8 MPa for the cortex (Fig. 2b), which is one to two orders of magnitude higher than the previously reported value obtained by AFM[27,28]. This is probably due to the high frequency of our mechanical measurement (~1 MHz) compared with the conventional frequency range of AFM operation (1–100 Hz) and a power-law relationship between the apparent elastic modulus (E) and the frequency (f): $E \propto f^{0.2-0.3}$ (ref. [29]). In agreement with our results, a similar value was reported with other high-frequency stiffness measurements of red blood cells[30]. Next, to correct for the cell-size dependence of the node deviation measurement (Fig. 1f), we derived the size-normalized acoustic scattering (SNACS) from the isoelasticity lines obtained from the FEM simulations (Fig. 2b, Supplementary Fig. 4). The isoelasticity lines fit well with the measurements from hundreds of live cells. The FEM

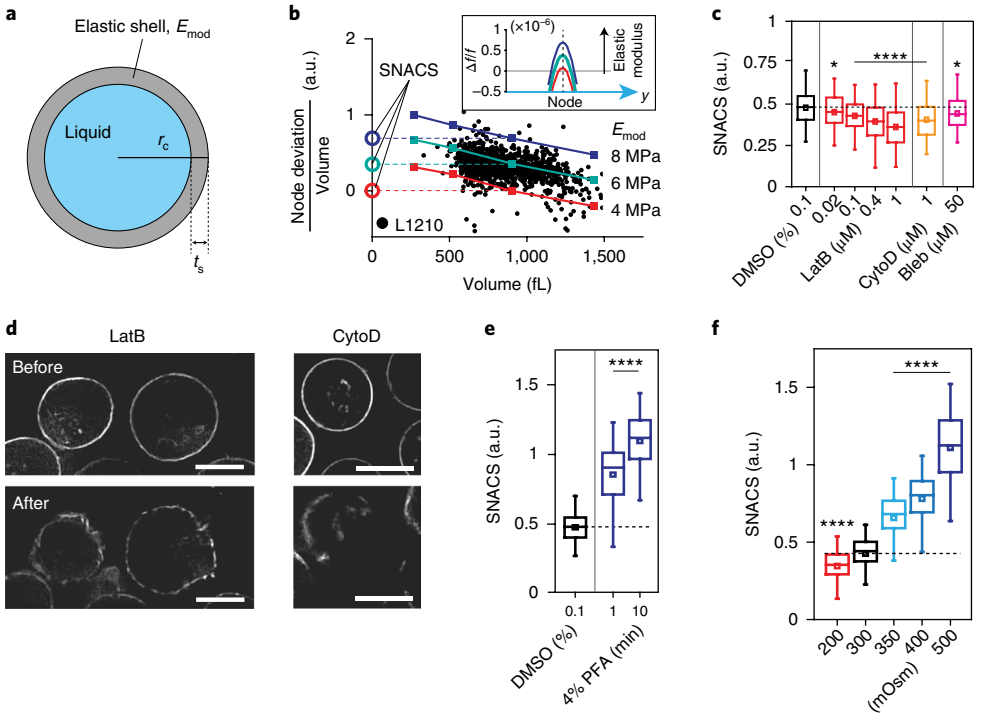

Fig. 2 | SNACS measures changes in the mechanical properties of cells. a, Schematic of the cortical shell–liquid core model, where E_{mod} is the elastic modulus of a shell. The cortical thickness (t_s) was set to 2% of the cell radius (r_c)[45]. **b**, Node deviation (volume-normalized) versus volume V from experiments with L1210 cells (black dots) and simulations using the model for three values of cortical elastic modulus (E_{mod}; 4, 6 and 8 MPa; colored lines). Vertical offsets of isoelasticity lines define SNACS (Methods). Inset, $\Delta f/f$ from simulations with different cortical elastic moduli (4, 6 and 8 MPa; $V = 900$ fL). **c**, SNACS obtained from L1210 cells treated with inhibitors of actomyosin cortex: latrunculin B (LatB; 0.02, 0.1, 0.4 and 1 μM; $n = 381$, 385, 346 and 383 cells, respectively; $P = 0.036$, 3.8×10^{-5}, 1.03×10^{-8} and 4.5×10^{-18}, respectively), cytochalasin D (CytoD; 1 μM; $n = 332$ cells; $P = 1.2 \times 10^{-8}$) and blebbistatin (Bleb; 50 μM; $n = 349$ cells; $P = 0.023$). Statistical comparisons (two-sided Welch's t-test) were made to the DMSO-treated control (0.1%; $n = 337$ cells). **d**, Representative single z-layer images of F-actin (LifeAct) from live L1210 cells before and after treatment with 1 μM LatB ($n = 9$ fields of view) and 1 μM CytoD ($n = 12$ fields of view). Scale bars, 10 μm. **e**, SNACS of L1210 cells after cross-linking with 4% paraformaldehyde (PFA; 1-min and 10-min exposure; $n = 247$ and 367 cells, respectively; $P = 2.0 \times 10^{-56}$ and 6.7×10^{-175}, respectively). Statistical comparisons (two-sided Welch's t-test) were made to the DMSO-treated control (0.1%; $n = 1{,}047$ cells). **f**, Effect of osmotic stress on SNACS. Cells were resuspended in hypo- (200 mOsm; $n = 611$ cells; $P = 2.9 \times 10^{-10}$) or hyperosmotic (350, 400 and 500 mOsm; $n = 544$, 571 and 574 cells, respectively; $P = 8.1 \times 10^{-65}$, 2.6×10^{-144} and $< 10^{-200}$, respectively) media. Statistical comparisons (one-way ANOVA, Fisher's least significant difference) were made to iso-osmotic (300 mOsm; $n = 539$ cells) media. Box plots in **c**,**e**,**f** denote the interquartile range (box hinges), means (squares), 5th and 95th percentiles (whiskers), and the mean SNACS of controls (DMSO or 300 mOsm; horizontal dashed lines); $^*P < 0.05$, $^{****}P < 0.0001$.

simulations indicated that SNACS increased with the elastic modulus of the cortex (E_{mod}; Fig. 2b, inset), as well as with cortical thickness (t_s), but was insensitive to both intracellular pressure and cortical tension (Supplementary Fig. 5). We also tested three other mechanical models, but none of them matched well with our observations (Supplementary Table 3). These results are in agreement with previous observations showing that small deformations primarily reveal mechanical properties of the cell cortex[28,31].

To experimentally determine whether SNACS correlates with mechanical properties of live cells, we examined SNACS after chemical perturbations. All actomyosin inhibitors tested decreased SNACS (Fig. 2c). We also generated an L1210 cell line that stably expresses the LifeAct–RFP F-actin probe[32]. We imaged these cells and observed that the chemical inhibitors of actin polymerization caused either a punctured cortex (latrunculin B) or a polarized cortex (cytochalsin D) (Fig. 2d). Both of these cortex phenotypes yielded a reduction in SNACS (Fig. 2c) that was substantially more than our system noise (Supplementary Fig. 6). We also observed reduced SNACS after microtubule-perturbing nocodazole treatment, but this treatment also affected the actin cortex morphology (Supplementary Fig. 7). We observed the opposite change in SNACS when we cross-linked cellular structures via a 1–10-min exposure to 4% paraformaldehyde (Fig. 2e). Moreover, when we perturbed cells osmotically, SNACS changed with the applied osmotic pressure (Fig. 2f). Notably, these perturbations resulted in SNACS changes (Fig. 2c–f) that are consistent with previous experiments in which stiffness was measured by a wide range of methods[9,10,13,14,33,34]. Thus, together with the hydrogel results (Fig. 1g) and FEM simulations, these results show that SNACS measures stiffness.

SNACS remains stable during interphase but is dynamic during mitosis. Next, we asked whether both the SNACS and the buoyant mass of a given cell could be repeatedly measured throughout the cell cycle. To do this, we implemented a previously reported fluidic control strategy that enables continuous, noninvasive SMR measurements of a single cell[35]. We simultaneously measured the SNACS and the buoyant mass of the same cell over multiple generations (Fig. 3a). Interdivision times measured by the SMR during the SNACS measurements were unchanged from those of bulk culture (Supplementary Fig. 8), which suggested that our measurement was not invasive. We observed that individual cells displayed stable SNACS throughout interphase, exhibiting significantly lower variability than what is seen across different cells in interphase (Fig. 3b). This suggests that cell-to-cell variability in cell mechanical properties during interphase arises not from cell-cycle-dependent

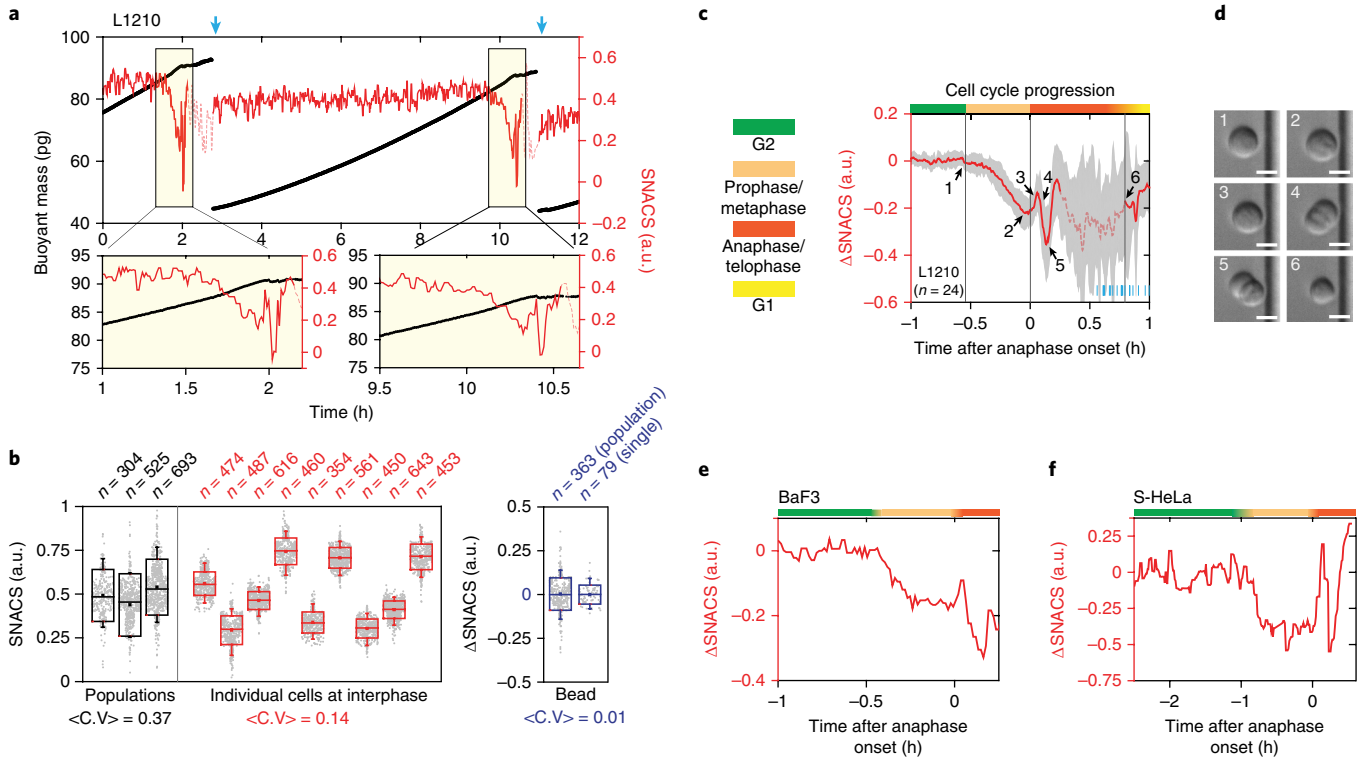

Fig. 3 | Continuous monitoring of single-cell SNACS throughout the cell cycle. a, Top, the buoyant mass (black) and SNACS (red) of an L1210 cell measured over two cell divisions with < 1-min temporal resolution by flowing of the cell back and forth through the SMR. Blue arrows mark cell division. Bottom, SNACS near mitosis. SNACS is indicated by dashed lines in regions where measurement error was statistically significant (Methods). **b**, SNACS variability during interphase at a cell-population level (black), in individual cells (red) and for 12-μm polystyrene beads (blue). Bead SNACS is shown relative to its mean value. Large (mitotic) cells were removed from the population data. <C.V> is the average coefficient of variation. *n* is the number of cells (black) or beads (blue) measured from each population or the number of repeated measurements during interphase of each individual cell (red) or bead (blue). Box edges indicate ± s.d., squares represent means, and whiskers extend to the 5th and 95th percentiles. **c**, Mean SNACS (red) and ± s.d. (gray) of L1210 cells during mitosis ($n = 24$ cells from 13 independent experiments). Vertical lines and color bars indicate the phase of the cell cycle. Short blue vertical lines at the bottom right mark the end of cell division for each cell. Dashed red lines are defined as in **a**. **d**, Representative morphology of an L1210 cell ($n = 24$ cells from 13 independent experiments) captured by differential interference contrast imaging on the SMR chip. Numbering corresponds to arrows in **c**. Scale bars, 10 μm. **e**,**f**, SNACS in mammalian BaF3 (**e**) and S-HeLa (**f**) cells. Color-coding defined as in **c**.

variability, but rather from mechanical differences that accumulate over generations.

In contrast to the interphase cells, mitotic cells showed large changes in SNACS (Fig. 3c). Using on-chip microscopy to acquire differential interference contrast images, we imaged the morphology of the cells to pinpoint the onset of anaphase (Fig. 3d) and correct for mass elongation effects on the SNACS measurement during anaphase and telophase (Supplementary Fig. 9, Supplementary Table 4 and Supplementary Notes 3 and 4). SNACS decreased gradually during early mitosis (but not in G2), abruptly increased at the onset of anaphase and then underwent a rapid decrease and recovery (Fig. 3c and Supplementary Fig. 10a,b). The error in the SNACS measurement increased after cells became full doublets (~15 min after the onset of anaphase), making subsequent SNACS changes until division not statistically significant ($P > 0.05$, two-sided Welch's *t*-test; Fig. 3c). Although the duration and magnitude of the SNACS dynamics varied in other mammalian cells (Fig. 3e, f), we observed similar trends.

Mitotic swelling is responsible for the SNACS decrease in early mitosis. Given that SNACS scales inversely with swelling (Fig. 2f), we hypothesized that mitotic swelling occurring in prophase and metaphase[36,37] might be responsible for the gradual decrease in SNACS. To test this hypothesis, we first correlated the timing of the mitotic swelling and the change in SNACS by simultaneously measuring SNACS and cell volume. Briefly, we consecutively weighed cells in two fluids of different densities to derive the single-cell volume, density and mass by means of a previously described technique[37]. When we combined this technique with the SNACS measurement, we observed that the SNACS decreased concomitantly with mitotic swelling (Fig. 4a). We further validated this by arresting cells in metaphase, where mitotic swelling is at a maximum[37], using the kinesin inhibitor S-trityl-L-cysteine (STLC). After mitotic entry, STLC-treated cells showed changes in SNACS similar to those seen during mitotic swelling of untreated cells (Fig. 4b, c). However, with STLC treatment, SNACS remained low for several hours (Fig. 4b). These results suggest that SNACS decreases concomitantly with mitotic swelling during prophase and metaphase, and further confirm that the subsequent increase in SNACS happens after metaphase.

We next acquired causative evidence that mitotic swelling causes the reduction in SNACS during prophase and metaphase. Previously we showed that inhibition of the Na^+/H^+ antiporter with ethylisopropylamioride (EIPA) reduces mitotic swelling without inhibiting mitosis[37]. Here we found that after EIPA treatment, SNACS in early mitosis was no longer reduced to the same extent as in the control cells and cells arrested in metaphase (Fig. 4c and Supplementary Fig. 10c). ΔSNACS of EIPA-treated cells in early mitosis was −0.08 ± 0.02 ($n = 5$ cells; all values are mean ± s.e.m. unless stated otherwise), whereas ΔSNACS of control cells and cells arrested in metaphase was −0.22 ± 0.01 ($n = 24$ cells) and 0.24 ± 0.03 ($n = 7$ cells), respectively.

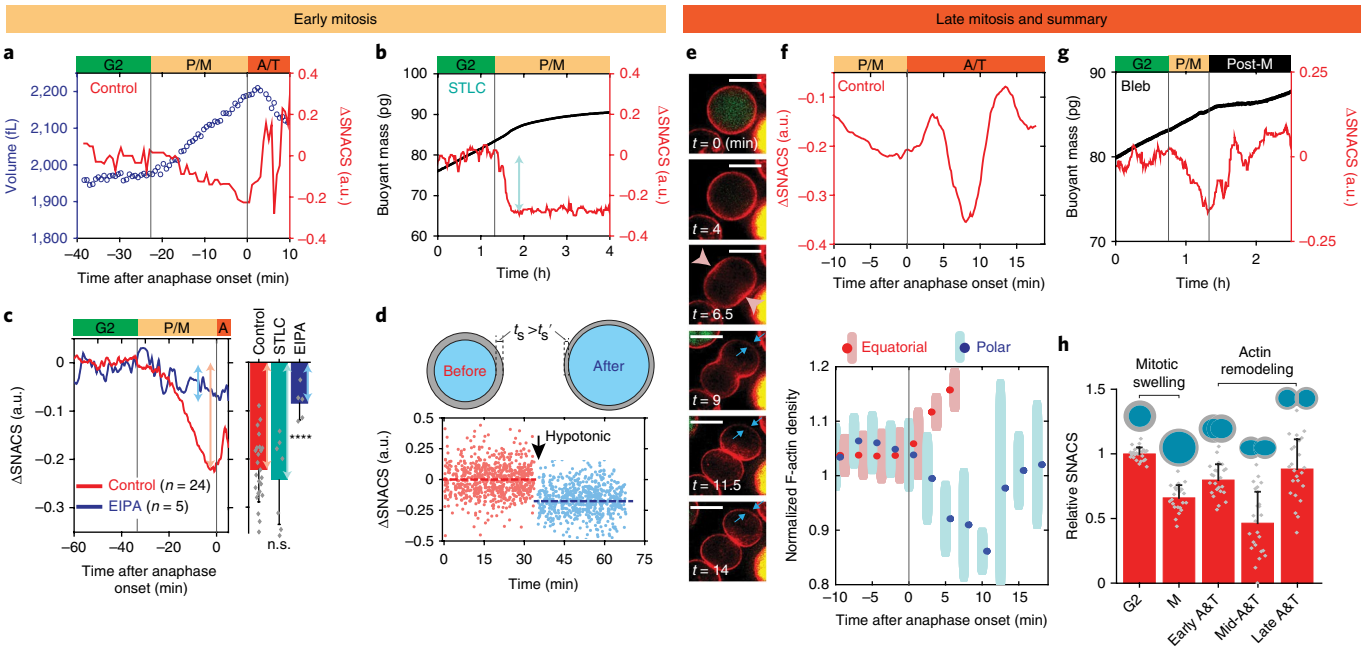

Fig. 4 | Mitotic swelling and actin remodeling are responsible for SNACS dynamics in mitosis. a, L1210 cell volume (blue circles) and SNACS (red) in mitosis. **b**, Buoyant mass (black) and SNACS (red) of an L1210 cell arrested in metaphase by treatment with STLC (5 μM). **c**, Left, mean SNACS change of control and EIPA-treated (10 μM) L1210 cells in early mitosis. Right, quantification of SNACS change with STLC (5 μM; $n = 7$ cells from 7 independent experiments; $P = 0.58$) and EIPA (10 μM; $n = 5$ cells from 5 independent experiments; $P = 3.0 \times 10^{-5}$) treatment. Data shown are the mean and s.d. of the maximal SNACS change in prophase and metaphase. Statistical comparisons (two-sided Welch's *t*-test) were made to the control ($n = 24$ cells from 13 independent experiments). ****$P < 0.0001$; n.s., not significant. **d**, Top, illustration of hypothetical cortical thinning by shell expansion during swelling (Supplementary Note 5). Bottom, SNACS of L1210 cells versus time before (red; $n = 728$ cells) and after (−Δ50 mOsm; blue; $n = 733$ cells) exposure to hypotonic stress. Dashed lines represent the mean SNACS of each condition. The arrow marks the time of osmotic shock. **e**, Representative single *z*-layer images of F-actin (red; LifeAct) and FUCCI (green; mAG-hGem) from a live L1210 cell ($n = 7$ cells). Time 0 marks the onset of anaphase. Furrow initiation in the equatorial region (pink arrowheads) and cortical relaxation at the poles (blue arrows) are highlighted. Scale bars, 10 μm. **f**, Top, zoomed-in view of mean SNACS in late-mitotic L1210 cells ($n = 24$ cells). Bottom, L1210 cortical LifeAct signal density in equatorial (red) and polar (blue) regions (Methods), as shown in **e**. Data shown are the mean ± s.d. of $n = 7$ cells. **g**, Buoyant mass (black) and SNACS (red) of an L1210 cell treated with blebbistatin (Bleb; 25 μM). **h**, Summary of SNACS dynamics in mitosis. Data shown are the mean ± s.d. of the SNACS normalized to G2 ($n = 24$ cells). Actin (gray shell) and morphology of a cell at each time point of mitosis are illustrated. **a**–**c**,**f**,**g**, Vertical lines separate the cell cycle positions marked by color bars shown in Fig. 3c. P, prophase; M, metaphase; A, anaphase; T, telophase.

These findings suggest that mitotic swelling is largely responsible for the reduction in SNACS. To determine whether swelling without a mitotic event can decrease SNACS, we induced swelling with a hypotonic shock (−Δ50 mOsm) in nonmitotic (interphase) cells. Immediately after the osmotic shock, cell volume increased by ~15%, as normally observed in mitotic swelling[37], and SNACS was reduced by a similar magnitude (ΔSNACS = −0.18 ± 0.01, $n = 733$ cells) as that seen during mitotic swelling (Fig. 4d). To mimic the gradual swelling during mitosis and potentially prevent membrane detachment from the cortex[33], we compared fast and slow swelling (−Δ50 mOsm instantaneously or over 20 min) and noted that the swelling rate did not affect the SNACS decrease (Supplementary Fig. 11). We hypothesized that swelling reduces cortical thickness by changing the hydrostatic pressure, thereby expanding actin to cover a larger surface area (Supplementary Note 5). We estimated that swelling of ~15% would lead to an ~10% decrease in cortex thickness, assuming that the amount of cortical actin did not change during swelling (Supplementary Table 5). We used live-cell fluorescent microscopy and found that the cortex thickness gradually decreased during mitotic swelling by an amount similar to our calculation (~10%) after nuclear envelope breakdown but before the onset of anaphase (Supplementary Figs. 12 and 13), in agreement with previous studies[1,38]. Altogether, these data suggest that mitotic swelling is responsible for cortical thinning and the consequent decrease in SNACS.

SNACS reveals mechanical changes during actin remodeling in late mitosis. We investigated the rapid SNACS change during anaphase and telophase (Fig. 3c). First, we observed that the SNACS increase in early anaphase (Fig. 4a,c, red) was not present in EIPA-treated samples (Fig. 4c, blue, and Supplementary Fig. 10c), which suggests that the SNACS increase represents recovery from mitotic swelling. To link mechanical dynamics to actin remodeling, we imaged changes in actin cortex distribution during anaphase and telophase (Fig. 4e and Supplementary Fig. 14). In early anaphase (~5 min after the onset of anaphase), where SNACS initially increases, cells started to elongate, and the cleavage furrow was initiated. At approximately 10 min into anaphase, where SNACS decreased, cells redistributed their cortical actin out of the polar regions. This polar relaxation[2] caused 10–15% depletion of F-actin at the poles and lasted approximately 5 min (Fig. 4f and Supplementary Fig. 12). Both SNACS and polar relaxation were recovered approximately 15 min after the onset of anaphase (Fig. 4f). When we inhibited cytokinesis and actin remodeling using the myosin II motor inhibitor blebbistatin, cells still showed a gradual SNACS decrease in early mitosis caused by mitotic swelling, but the mechanical dynamics in anaphase and telophase seen in untreated cells were not observed (Fig. 4g). These observations reveal how cortical thinning induced by mitotic swelling in early mitosis and actin remodeling, especially polar relaxation, in late mitosis result in dynamic changes in cellular mechanical properties (Fig. 4h).

Discussion

It is known that during early mitosis, when SNACS decreases, cells swell, the actin cortex thickness is reduced and cortical tension is increased[1,38], yet prior work on how stiffness changes has not been consistent. It has been thought that mitotic cells become stiffer because of increased tension[39] from contractility in the membrane during mitotic roundup. Results of early AFM[40] and optical tweezer[41] experiments on cells in mitosis supported this notion. The SNACS decrease we observed could have resulted from reductions in both cortex thickness and modulus. However, a separate study using AFM found no change in mitotic stiffness[42], whereas others using hydrodynamic forces have observed that mitotic cells become more deformable[43]. All of these studies[40–43] were conducted as end-point assays on different cell types with strains that were 10- to 100-fold larger than those used during our SNACS measurement. Future work will be necessary to determine how the cortex tension, modulus and thickness govern cell stiffness dynamics during mitosis. Aside from the cortex, it remains plausible that SNACS reflects other attributes of the cell such as the plasma membrane and the way in which it is attached to the underlying cortex.

We also found that SNACS recovered from cell swelling at the onset of anaphase, and then decreased during anaphase and telophase. Early work on the mechanical properties of sea urchin eggs suggested similar dynamic changes in anaphase[44]. This reduction in SNACS was dependent on actomyosin remodeling and coincided with the polar relaxation of actin cortex[2].

Finally, our SNACS measurement is influenced by the cell's mass distribution along the cantilever. During anaphase and telophase, a cell's mass distribution changes substantially, which causes the SNACS measurement to depend on the cell's orientation within the channel (Supplementary Fig. 15, Supplementary Note 4 and Supplementary Table 4). Therefore, to obtain mechanical measurements by acoustic scattering, one needs to acquire mass distribution information from bright-field images, unless the cell shape is known a priori. In round interphase cells, such as the ones we studied here, this correction is not required.

We have shown that the continuous measurement of single-cell mechanical properties with high temporal resolution over extended periods is critical for observation of small changes that are both transient and asynchronous between cells. We demonstrated this by measuring mitotic-specific mechanical changes that were smaller than the population variance and that occurred within minute time scales. Our SNACS measurement quantifies the overall mechanical properties of a cell, complementing spatially resolved measurements such as time-lapse microscopy, traction force microscopy and AFM.

Online content

Any methods, additional references, Nature Research reporting summaries, source data, statements of data availability and associated accession codes are available at https://doi.org/10.1038/s41592-019-0326-x.

Received: 13 September 2018; Accepted: 9 January 2019;
Published online: 11 February 2019

References

1. Chugh, P. et al. Actin cortex architecture regulates cell surface tension. *Nat. Cell Biol.* **19**, 689–697 (2017).
2. Rodrigues, N. T. et al. Kinetochore-localized PP1-Sds22 couples chromosome segregation to polar relaxation. *Nature* **524**, 489–492 (2015).
3. Fletcher, D. A. & Mullins, R. D. Cell mechanics and the cytoskeleton. *Nature* **463**, 485–492 (2010).
4. Gardel, M. L., Schneider, I. C., Aratyn-Schaus, Y. & Waterman, C. M. Mechanical integration of actin and adhesion dynamics in cell migration. *Annu. Rev. Cell Dev. Biol.* **26**, 315–333 (2010).
5. Byun, S. et al. Characterizing deformability and surface friction of cancer cells. *Proc. Natl. Acad. Sci. USA.* **110**, 7580–7585 (2013).
6. Swaminathan, V. et al. Mechanical stiffness grades metastatic potential in patient tumor cells and in cancer cell lines. *Cancer Res.* **71**, 5075–5080 (2011).
7. Paluch, E. & Heisenberg, C. P. Biology and physics of cell shape changes in development. *Curr. Biol.* **19**, R790–R799 (2009).
8. Henderson, E., Haydon, P. G. & Sakaguchi, D. S. Actin filament dynamics in living glial cells imaged by atomic force microscopy. *Science* **257**, 1944–1946 (1992).
9. Radmacher, M. Studying the mechanics of cellular processes by atomic force microscopy. *Methods Cell Biol.* **83**, 347–372 (2007).
10. Ou-Yang, H. D. & Wei, M. T. Complex fluids: probing mechanical properties of biological systems with optical tweezers. *Annu. Rev. Phys. Chem.* **61**, 421–440 (2010).
11. Wang, N., Butler, J. P. & Ingber, D. E. Mechanotransduction across the cell surface and through the cytoskeleton. *Science* **260**, 1124–1127 (1993).
12. Lincoln, B., Wottawah, F., Schinkinger, S., Ebert, S. & Guck, J. High-throughput rheological measurements with an optical stretcher. *Methods Cell Biol.* **83**, 397–423 (2007).
13. Gossett, D. R. et al. Hydrodynamic stretching of single cells for large population mechanical phenotyping. *Proc. Natl. Acad. Sci. USA.* **109**, 7630–7635 (2012).
14. Otto, O. et al. Real-time deformability cytometry: on-the-fly cell mechanical phenotyping. *Nat. Methods* **12**, 199–202 (2015).
15. Brangwynne, C. P., MacKintosh, F. C. & Weitz, D. A. Force fluctuations and polymerization dynamics of intracellular microtubules. *Proc. Natl. Acad. Sci. USA.* **104**, 16128–16133 (2007).
16. Gupta, S. K. & Guo, M. Equilibrium and out-of-equilibrium mechanics of living mammalian cytoplasm. *J. Mech. Phys. Solids.* **107**, 284–293 (2017).
17. Tseng, Y., Kole, T. P. & Wirtz, D. Micromechanical mapping of live cells by multiple-particle-tracking microrheology. *Biophys. J.* **83**, 3162–3176 (2002).
18. Matzke, R., Jacobson, K. & Radmacher, M. Direct, high-resolution measurement of furrow stiffening during division of adherent cells. *Nat. Cell Biol.* **3**, 607–610 (2001).
19. Guillou, L., Babataheri, A., Puech, P. H., Barakat, A. I. & Husson, J. Dynamic monitoring of cell mechanical properties using profile microindentation. *Sci. Rep.* **6**, 21529 (2016).
20. Wang, H. et al. Acoustophoretic force-based compressibility measurement of cancer cells having different metastatic potential. *Proc. Meet. Acoust.* **19**, 045019 (2013).
21. Yang, T. et al. A comprehensive strategy for the analysis of acoustic compressibility and optical deformability on single cells. *Sci. Rep.* **6**, 23946 (2016).
22. Hartono, D. et al. On-chip measurements of cell compressibility via acoustic radiation. *Lab Chip* **11**, 4072–4080 (2011).
23. Burg, T. P. et al. Weighing of biomolecules, single cells and single nanoparticles in fluid. *Nature* **446**, 1066–1069 (2007).
24. Dohn, S., Svendsen, W., Boisen, A. & Hansen, O. Mass and position determination of attached particles on cantilever based mass sensors. *Rev. Sci. Instrum.* **78**, 103303 (2007).
25. Yeung, A. & Evans, E. Cortical shell-liquid core model for passive flow of liquid-like spherical cells into micropipets. *Biophys. J.* **56**, 139–149 (1989).
26. Lim, C. T., Zhou, E. H. & Quek, S. T. Mechanical models for living cells—a review. *J. Biomech.* **39**, 195–216 (2006).
27. Fischer-Friedrich, E. et al. Rheology of the active cell cortex in mitosis. *Biophys. J.* **111**, 589–600 (2016).
28. Cartagena-Rivera, A. X., Logue, J. S., Waterman, C. M. & Chadwick, R. S. Actomyosin cortical mechanical properties in nonadherent cells determined by atomic force microscopy. *Biophys. J.* **110**, 2528–2539 (2016).
29. Balland, M. et al. Power laws in microrheology experiments on living cells: comparative analysis and modeling. *Phys. Rev. E* **74**, 021911 (2006).
30. Wang, A., Vijayraghavan, K., Solgaard, O. & Butte, M. J. Fast stiffness mapping of cells using high-bandwidth atomic force microscopy. *ACS Nano* **10**, 257–264 (2016).
31. Ananthakrishnan, R. et al. Quantifying the contribution of actin networks to the elastic strength of fibroblasts. *J. Theor. Biol.* **242**, 502–516 (2006).
32. Riedl, J. et al. Lifeact: a versatile marker to visualize F-actin. *Nat. Methods* **5**, 605–607 (2008).
33. Steltenkamp, S., Rommel, C., Wegener, J. & Janshoff, A. Membrane stiffness of animal cells challenged by osmotic stress. *Small* **2**, 1016–1020 (2006).
34. Guo, M. et al. Cell volume change through water efflux impacts cell stiffness and stem cell fate. *Proc. Natl. Acad. Sci. USA.* **114**, E8618–E8627 (2017).
35. Son, S. et al. Direct observation of mammalian cell growth and size regulation. *Nat. Methods* **9**, 910–912 (2012).
36. Zlotek-Zlotkiewicz, E., Monnier, S., Cappello, G., Le Berre, M. & Piel, M. Optical volume and mass measurements show that mammalian cells swell during mitosis. *J. Cell. Biol.* **211**, 765–774 (2015).
37. Son, S. et al. Resonant microchannel volume and mass measurements show that suspended cells swell during mitosis. *J. Cell. Biol.* **211**, 757–763 (2015).

38. Ramanathan, S. P. et al. Cdk1-dependent mitotic enrichment of cortical myosin II promotes cell rounding against confinement. *Nat. Cell Biol.* **17**, 148–159 (2015).
39. Stewart, M. P. et al. Hydrostatic pressure and the actomyosin cortex drive mitotic cell rounding. *Nature* **469**, 226–230 (2011).
40. Kunda, P., Pelling, A. E., Liu, T. & Baum, B. Moesin controls cortical rigidity, cell rounding, and spindle morphogenesis during mitosis. *Curr. Biol.* **18**, 91–101 (2008).
41. Matthews, H. K. et al. Changes in Ect2 localization couple actomyosin-dependent cell shape changes to mitotic progression. *Dev. Cell.* **23**, 371–383 (2012).
42. Jiang, N. et al. Probing the biophysical properties of tumor cells during mitosis by atomic force microscopy. *Biomech. Model. Mechanobiol.* **17**, 1209–1215 (2018).
43. Rosendahl, P. et al. Real-time fluorescence and deformability cytometry. *Nat. Methods* **15**, 355–358 (2018).
44. Hiramoto, Y. Mechanical properties of the surface of the sea urchin egg at fertilization and during cleavage. *Exp. Cell Res.* **89**, 320–326 (1974).
45. Clark, A. G., Dierkes, K. & Paluch, E. K. Monitoring actin cortex thickness in live cells. *Biophys. J.* **105**, 570–580 (2013).

Acknowledgements

We thank K. Elias (Brigham and Women's Hospital) for S-HeLa cells, and E. Vasile and the Koch Institute microscopy core, which is partly funded by Koch Institute Support Grant P30-CA14051 from the National Cancer Institute, for technical support. This work was funded in part by the Ludwig Center for Molecular Oncology (S.R.M.), the Cancer Systems Biology Consortium U54 CA217377 from the NCI (S.R.M.), and the Institute for Collaborative Biotechnologies through grant W911NF-09-0001 from the US Army Research Office (S.R.M.). T.P.M. is supported by the Wellcome Trust (Sir Henry Postdoctoral Fellowship grant 110275/Z/15/Z). J.H.K. acknowledges support from a Samsung scholarship.

Author contributions

J.H.K. and S.R.M. conceptualized the study. J.H.K., with assistance from S.O., G.K. and S.R.M., designed the modeling and experiments done with beads. J.H.K. and T.P.M. designed the experiments with cells. J.H.K. performed all node deviation experiments and analyzed the data. J.H.K., with assistance from G.K., carried out the modeling. T.P.M. carried out all imaging experiments. S.O., with assistance from J.H.K. and T.P.M., carried out the image analysis. L.C. and P.S.D. created the hydrogel particles. T.P.M. and S.R.M. supervised the study. J.H.K., T.P.M., G.K. and S.R.M. wrote the paper with input from all other authors.

Competing interests

S.R.M. is a founder of Travera and Affinity Biosensors.

Additional information

Supplementary information is available for this paper at https://doi.org/10.1038/s41592-019-0326-x.

Reprints and permissions information is available at www.nature.com/reprints.

Correspondence and requests for materials should be addressed to S.R.M.

Publisher's note: Springer Nature remains neutral with regard to jurisdictional claims in published maps and institutional affiliations.

Methods

System setup. SMR devices were fabricated via a previously described process[23,46] carried out at CEA-LETI (Grenoble, France). The geometry and dimensions of SMR devices used in the experiments described in this work are shown in Supplementary Fig. 1 and Supplementary Table 2. The measurement system for trapping a cell throughout its cell cycle is described in ref. [35]. The SMRs were vibrated with a piezo-ceramic plate bonded underneath the chip, providing actuation to resonate the cantilever beam in the second mode. To track the changes in the resonant frequency of the cantilever as a function of time, we used a closed feedback loop to drive the cantilever to always oscillate at its resonant frequency. The motion of the cantilever was measured with piezoresistors implanted at the base of the silicon cantilever[47]. A previously reported[48] digital control platform was used to oscillate the SMR in direct feedback mode, where the motion signal acquired from the piezoresistor is delayed, amplified and used as the drive signal to actuate the cantilever. We set the measurement bandwidth of this control system at ~1,500 Hz, which is wide enough to capture frequency modulation signals created by cell transit events and narrow enough to minimize noise.

For on-chip optical measurements, a modular microscope (Nikon) was mounted on top of the SMR device. A 20×/0.4-NA (numerical aperture) objective lens (Nikon-CFI, LU Plan ELWD WD 13 mm) or 50×/0.55-NA objective lens (Nikon-CFI, LU Plan ELWD WD 10.1 mm) was used to collect light into a CMOS (complementary metal-oxide semiconductor) camera (FLIR, BFS-U3–13Y3M-C) or photomultiplier tube (Hamamatsu, H10722–20), respectively, in order to obtain differential interference contrast (DIC) images or measure fluorescent intensity. The field of view and area of light exposure were typically reduced to 100×100 µm (DIC imaging) or 40×60 µm (fluorescent measurements) to minimize the background noise and phototoxicity. To further improve the signal-to-noise ratio, we adjusted a rectangular slit (Thorlab) to fit the channel width and placed it at the image plane. An illumination light source (Lumencor, Spectra X Light Engine) was shuttered by the measurement software (Labview 2012) to excite each fluorescent measurement for less than 550 ms. The optical path and components for imaging and fluorescent measurements were similar to what has been described previously[35].

System operation. As previously reported[37], a chip was placed on top of a hollow copper plate connected to a water bath by tubing to maintain constant temperature on the chip. For all long-term single-cell monitoring experiments, the temperature of the copper plate was kept at 37 °C. The sample was loaded to the SMR from vials pressurized with air containing 5% CO_2 to maintain the pH of the culture. We used 0.007-inch-inner-diameter fluorinated ethylene propylene tubing (IDEX Health & Science) to push the sample into the chip. The fluid flow was controlled by two electronic pressure regulators (Proportion Air QPV1) and three solenoid valves (SMC-S070), which were controlled by National Instruments control cards and a custom measurement software (LabVIEW 2012). Typically, differential pressure of ~0.5 p.s.i. was applied across the SMR, yielding a flow rate of ~2 nl/s (calculated on the basis of the frequency modulation signal during a cell transit; typically 200–300 ms) to maintain constant shear and data rate. Under these conditions, the L1210 cell growth rate was similar to that in culture[35]. Beads, hydrogels and drug-response end-point assays were measured at room temperature. All end-point assays were conducted within 30 min after samples were loaded. New samples were flushed every several minutes into the input bypass to minimize potential size bias due to particle or cell settling in the tubing and sample vials.

Frequency peak analysis. To measure buoyant mass (antinode) and node deviation (node) from the acquired resonant frequency waveforms, we filtered the frequency data with a third-order Savitzky–Golay low-pass filter and found the local minima (antinode) that were below a user-defined threshold. Next, local maxima (node) around the peaks were determined. Then, to correct for the possible slope during the particle or cell transition through the cantilever, we calculated a baseline and subtracted it from the measured peaks by fitting a first-order polynomial at frequency data points prior and posterior to the cell signal. Typically, we acquire frequency data for ~1 s before and after the transit of each cell to estimate the baseline frequency. As a result, the measurement time is typically 2–3 s per cell, which leads to a throughput of about 1,200 cells per hour (accounting for occasional doublets and delays between cell measurements). For single-cell volume measurements (Fig. 4a), baselines were fitted with a second-order polynomial to account for the baseline fluctuation due to fluid exchange. We subtracted both local maxima and minima in the cell signal from the linear baseline to obtain the buoyant mass (local minima, antinode) and node deviation (local maxima, node). For single-cell end-point assays (population measurements), frequency peaks were rejected when local minima (two antinodes) differed from each other by more than 10% of the average value and/or local maxima (two nodes) differed from each other by more than 15% of the average value of local minima, which occurred when multiple cells or a cell with debris entered the SMR simultaneously. Peaks were rejected if their shape was atypical (e.g., because of a particle or cell stuck in the cantilever). For single-cell long-term monitoring, all frequency peaks were accepted and presented except extremely rare events such as when a doublet separated into two daughter cells during the transit through the cantilever or entered apoptosis because of persistent drug pressure. Frequency peaks were calibrated (Hertz per picogram) using monodisperse 10-µm-diameter polystyrene beads with a known density of 1.05 g/cm^3 (Thermo Fisher, Duke Standards).

Hydrogel particle synthesis. Hydrogel microparticles were fabricated via stop-flow lithography (SFL)[49,50]. Microfluidic synthesis devices were fabricated by previously reported procedures[2]. Briefly, PDMS (10:1 monomer to curing agent; Sylgard 184; Dow Corning) was cured on silicon wafers patterned with SU-8 features, and devices were bonded to PDMS-coated glass slides. We prepared prepolymer solutions by mixing 20% (v/v) poly(ethylene glycol) diacrylate (PEGDA; Mn = 700; Sigma-Aldrich), 5% 2-hydroxy-2-methyl-propiophenone (photoinitiator; Sigma-Aldrich), 25% deionized water, and 50% PEG (Mn = 200; Sigma-Aldrich).

Using the previously reported SFL setup[49,50], we loaded prepolymer solution into the synthesis device by pressure-controlled flow. After the flow was stopped, particles were polymerized by ultraviolet light (Thorlabs; 365-nm LED; 2,200 mW/cm^2) in mask-defined shapes (transparency masks designed in AutoCAD, printed by Fineline Imaging). The three steps (flow, stop and exposure) were repeated to achieve semi-continuous particle synthesis. Polymerized particles were collected from the channel outlet and purified with PBST (PBS with 0.05% Tween 20) by centrifugation.

Hydrogel microparticles with varying elastic moduli (Fig. 1g) were synthesized using the SFL setup. Prepolymer solutions were prepared with varying concentrations of PEGDA (Mn = 700) in the range of 10–35% (v/v), plus 5% photoinitiator, 25% deionized water, and PEG (Mn = 200) in the range of 35–60% to make up the remaining volume. For all prepolymer compositions, particles were polymerized with an 11-µm circle mask in microfluidic channels with heights of 10 µm, which resulted in particle heights of 7–8 µm.

We fabricated hydrogels of three aspect ratios—1.0, 1.5 and 2.5 (Supplementary Fig. 3)—by using three masks with the same cross-sectional area for exposure, but three different shapes, respectively: an 11-µm-diameter circle, an ellipse with aspect ratio 1.5 (major axis:minor axis), and an ellipse with aspect ratio 2.5. The volumes of hydrogels were measured by dynamic light scattering with means of 655, 658 and 602 µm^3 for aspect ratios of 1, 1.5 and 2.5, respectively. Particle dimensions (height and major/minor axes) were measured from bright-field microscopy images with ImageJ software, using an average from at least ten particles.

Measurement of particle elastic modulus by atomic force microscopy. To determine the elastic modulus of the hydrogel microparticles, we carried out force spectroscopy measurements using an MFP-3D-BIO atomic force microscope with an integrated optical microscope (Asylum Research). A 50-µl drop of particle solution (approximately ten particles in PBST) was placed on a glass slide. Silicon nitride cantilevers with silica spherical indenters of 10-µm diameter (Novascan) were used to indent the particles in PBST after they settled to the surface of the slide. For particles with composition 10–25% PEGDA, a cantilever with a nominal spring constant of 0.12 N/m was used. For stiffer particles with a higher (30–35%) PEGDA composition, a cantilever with a nominal spring constant of 0.35 N/m was used. The inverse optical lever sensitivity for each cantilever was calibrated from deflection-displacement curves on a rigid glass slide (23.21 and 17.46 nm/V, respectively), and the actual spring constant of each cantilever was measured via the thermal noise method[51] as 0.114 and 0.475 N/m, respectively. For each sample, we indented four particles with four indents per particle. We calculated the elastic modulus by fitting the force-indentation curves to a maximum indentation depth of 400 nm using the Hertz model for spherical elastic contact with IGOR data processing software (Wavemetrics). The indentation velocity was 1 µm/s. The PEGDA hydrogels were assumed to be incompressible elastic materials with a Poisson's ratio of 0.5 (refs. [52,53]).

Cell culture, chemical perturbations and transfections. L1210 and BaF3 cells were cultured in RPMI containing L-glutamine, phenol red and 11 mM D-glucose, and the RPMI was supplemented with 10% heat-inactivated FBS, 10 mM HEPES, 100 units/ml penicillin, 100 µg/ml streptomycin, and 0.25 µg/ml amphotericin B. S-HeLa cells were cultured in DMEM containing L-glutamine, phenol red, 25 mM D-glucose, and the DMEM was supplemented as RPMI. All cell culture reagents were obtained from Thermo Fisher Scientific, except FBS, which was obtained from Sigma-Aldrich. The L1210 cells were obtained from ATCC (CCL-219). BaF3 cells expressing BCR-ABL were obtained from RIKEN BioResource center. S-HeLa cells were a gracious gift from Dr. Kevin Elias (Brigham and Women's Hospital). All experiments were started from cell cultures that had not reached more than 40% confluence.

For chemical perturbations, cells were pretreated with chemicals for 20–30 min under normal cell culture conditions and loaded into the SMR along with the chemical-containing media. Chemical concentrations used were 0.1% DMSO (controls; Sigma-Aldrich), 0.02–1 µM latrunculin B (Sigma-Aldrich), 1 µM cytochalasin D (Sigma-Aldrich), 25 µM (cytokinesis inhibition, long-term traces) or 50 µM (actomyosin cortex disruption, end-point assay) blebbistatin (Sigma-Aldrich), 10 µM EIPA (Sigma-Aldrich), 5 µM STLC (Sigma-Aldrich) and 2 µM RO3306 (R&D Systems). For surface cross-linking experiments, cells were treated with 4% PFA (Electron Microscopy Sciences) in PBS for 1 or 10 min. Cells were

then washed with PBS and resuspended in normal culture media. For all wash and resuspension steps, cells were centrifuged at 500 *g* for 2 min. For the osmotic challenge, we achieved the desired osmolarity of the external solutions by mixing cell culture media with deionized water or D-mannitol (Sigma-Aldrich) for hypotonic or hypertonic conditions, respectively. Cell culture media was set to be isotonic (300 mOsm). Cells in the culture media were mixed 1:1 with the prepared external solution (for example, mixed 1:1 with 500 mOsm solution to achieve a final osmolarity of 400 mOsm) to obtain the desired osmolarity. We kept the cells in the prepared media solution at room temperature for 20 min before loading them into an SMR containing media of the desired osmolarity. For the hypotonic experiment shown in Fig. 4d, cells were loaded immediately after the osmotic shock. For the slow hypotonic shock condition shown in Supplementary Fig. 11, cells were treated with deionized water every 2 min for a total of 20 min. We achieved the desired osmolarity of 250 mOsm by adding 10 µl of water every 2 min (a total of ten times) into 500 µl of cell solution.

L1210 FUCCI cells, which express the fluorescent cell-cycle marker construct mAG-hGem, were generated in a previous study[35]. These cells were transfected with LifeAct, an F-actin-labeling red fluorescent protein construct[32], using rLVUbi-LifeAct-TagRFP lentiviral vector obtained from ibidi GmbH. Several rounds of transfections were carried out via spinoculation. In short, 1.5×10^5 L1210 FUCCI cells were mixed with 10 µg/ml Polybrene (EMD Millipore) and 1×10^6 transducing units of lentivirus, and the mixture was centrifuged at 800 *g* for 60 min at 25 °C. After centrifugation, the cells were moved to normal cell culture media and grown overnight, and then the spinoculation procedure was repeated. After three rounds of transfection, cells were moved to normal culture media, and 24 h later we started the selection process by adding 10 µg/ml puromycin (Sigma-Aldrich). After a week of selection, the transfected population was enriched for cells expressing high levels of LifeAct by FACS sorting on a BD FACSAria.

Size-normalizing node deviation to obtain SNACS values. Because node deviation decreases with particle volume (Figs 1f and 2b), size normalization is required in order to compare the node deviation of different-size particles or cells. To obtain the SNACS, we first obtained the volume via a previously described method[5]. In short, we converted the buoyant mass obtained from individual peaks (Supplementary Fig. 4a) to volume by using a median density of the population. We obtained the median density of the population relative to the fluid ($\overline{\Delta\rho}=\overline{\rho_c-\rho_f}$) by fitting the buoyant mass distribution with a log-normal distribution to estimate the mean buoyant mass ($\overline{BM}$; > 300 cells). We obtained the mean volume ($\overline{V}$) by fitting the log-normal distribution to the volume distribution obtained from the Coulter Counter measurements (Beckman Coulter; > 5,000 counts). We then obtained the single-cell volume by using the following equation:

$$V=\frac{BM}{\overline{\Delta\rho}},\ \text{where}\ \overline{\Delta\rho}=\frac{\overline{BM}}{\overline{V}}$$

The mean density ($\overline{\Delta\rho}$) of the population was calculated for each condition. Then, the node deviation for each cell (Supplementary Fig. 4a) was divided by its volume (V) to obtain node deviation/volume (NV). With each cell represented as a data point in the scatter plot (NV versus V; Supplementary Fig. 4b), an isoelasticity line of slope m is passed through each point (Supplementary Fig. 4c). All data points along a given isoelasticity line have the same mechanical property based on the FEM simulation (Fig. 2b). Finally, we obtained the SNACS for each cell by taking the linear interpolation of NV at V_{ref} along the isoelasticity line (Supplementary Fig. 4d):

$$\text{SNACS}=NV-m(V_{ref}-V)$$

We obtained the slope (m) by carrying out linear regression on the population data (typically > 300 cells) in the NV-versus-V scatter plot (Fig. 2b). The reference volume (V_{ref}) was set as the median volume of the population, which for L1210 cells was 900 fL.

Cell-cycle transition points. To pinpoint the G2–metaphase transition, we used a previously reported finding that mitotic swelling starts in early prophase and prometaphase[37]. As the SNACS decrease was simultaneous with swelling (Fig. 4a) and was not observed in G2 arrested cells (Supplementary Fig. 10a), we marked the G2–prophase transition as taking place right before the SNACS decrease starts. The FUCCI signal (mAG-hGem) decrease (when fluorescence first reaches 85% of the maximum value) was used to mark the metaphase-to-anaphase transition. On the basis of fluorescence imaging, we obtained the average time lag between the time when the FUCCI signal (mAG-hGem) begins to drop (below 85% maximum) and the first time point for when a cell deviates from spherical as ~3.8 min. Then, to assign the cell-cycle transition points in figures, we subtracted the 3.8-min time lag from the first time point when cell shape deviates from spherical to mark the start of anaphase. SNACS traces of the metaphase arrested cells (treated with STLC), in which SNACS remained low for several hours, supported our timing of the metaphase–anaphase transition (Fig. 4b).

Microscopy. L1210 cells expressing the FUCCI (mAG-hGem) and LifeAct–RFP F-actin probe (rLVUbi-LifeAct-TagRFP) constructs were imaged on poly-lysine-coated glass-bottom CellView cell culture dishes (Greiner Bio-One). Media, CO_2 and temperature conditions during imaging were the same as within the SMR. Imaging was carried out on a DeltaVision wide-field deconvolution microscope with standard FITC and TRICT filters, a 100× oil-immersion objective, and immersion oil with a refractive index of 1.522. No binning was used and the image resolution was 9.245 pixels/µm in xy planes. When examining the effects of actin-perturbing chemicals on the F-actin structure, we imaged a 3-µm-thick section from the middle of the cells in 0.2-µm-thick z-layers. After the first round of imaging, the cells were treated with the indicated chemical for 30 min, and the same cells were imaged again. When examining the F-actin distribution in early mitosis, we imaged a 1-µm-thick section from the middle of the cells in 0.2-µm-thick z-layers every 5 min. Only the middle z-layer was used for final analysis and presentation. When examining the F-actin distribution during cytokinesis, we imaged three 0.2-µm-thick z-layers with 1-µm height intervals to capture both the mother and the daughter cells at the central height of the cell, and we repeated this imaging every 2.5 min. The total duration of all imaging experiments was limited to 5 h, as prolonged light exposure induced phototoxicity and started to interfere with mitotic progression.

Image analysis: actin cortex thickness in early mitosis. All images were deconvolved using standard settings in the softWoRX software. To normalize the effect of photobleaching, first we calculated the total LifeAct signal in the full images (2,048 × 2,048 pixels) that contained multiple cells. Then, we fitted a second-order polynomial to the total LifeAct signal in the image as a function of frame index. During the subsequent image analyses, we corrected the LifeAct intensity with the corresponding decay coefficient calculated from the polynomial fit for each frame. To analyze individual cells, we first identified the representative cells that went through the nuclear envelope breakdown and/or cytokinesis during the experiment. These cells were cut out of the larger images and analyzed individually (Supplementary Fig. 12a).

For analysis of each cell, we used MATLAB's circular Hough transform algorithm to detect circles on images ('imfindcircles'). We applied this algorithm to binary images that were processed by a two-dimensional median filter with a 3-by-3 neighborhood (Supplementary Fig. 12b) and a threshold filter (Supplementary Fig. 12c). After determining an initial position for the cell center and the radius (Supplementary Fig. 12d), we obtained the actin signal at the raw, unfiltered image across 100 radial paths around the detected circle ranging from the estimated cell center to 125% of the estimated cell radius (Supplementary Fig. 12e). Then, we recorded the prominent peak location of the actin signal that was closest to the estimated radius as the cortex position for that particular radial path. We took the median of LifeAct signals recorded from each radial path after aligning them at their calculated cortex locations (Supplementary Fig. 12f). Using this median LifeAct profile of the cell cross-section, we calculated the full width at half-maximum (FWHM) of the LifeAct signal at the cortex (Supplementary Fig. 12f, red circles) in reference to the LifeAct signal recorded at the cytoplasm. We defined the baseline signal at the cytoplasm of L1210 cells as approximately 85–90% of the radial measurement path (Supplementary Fig. 12f, red line). This FWHM value of LifeAct at the cortex functioned as a proxy for the cortex thickness.

To analyze F-actin distribution dynamics through mitosis, we repeated our analysis for each time point we collected throughout the experiment. At each time point we also analyzed the distribution of the FUCCI signal (mAG-hGem) in the cell (Supplementary Fig. 12g). We aligned the data from different cells to the time of nuclear envelope breakdown using the FUCCI signal (mAG-hGem) spread from nucleus to across the entire cell area as a marker for the nuclear envelope breakdown (Supplementary Fig. 12h). Finally, to compare different cells, we normalized the FWHM signals of each cell with respect to the median FWHM signal that was recorded from the frames of that cell before the nuclear envelope breakdown.

Image analysis: equatorial and polar actin cortex density during mitosis. To study how the distribution of F-actin changes through mitosis, we considered four regions of the cell. Each region covered a 90° area extending from 65% of the estimated radius of the cell to its full radius. We used the same cell-detection algorithm that was described in the previous section, with the additional capability of detecting two adjacent cells (Supplementary Fig. 12i,j). To determine the division axis and the regions of interest, we started the analysis from the frames after cytokinesis with two cells clearly visible, and worked back in time until the onset of anaphase. At each time point, if we detected two cells, even if the cell was in mid-anaphase, we determined the division axis and the equatorial and polar regions of interest. We set the polar region as the 90° segments that were at two opposite sides of the detected cells (Supplementary Fig. 12k). We set the equatorial region as the regions that were in the middle of the two cells and had an angular span perpendicular to the polar regions (Supplementary Fig. 12l). To compensate for the observed noncircular shapes, we used an edge detection algorithm to determine the true extent of the cells' overlap with the region of interest. If we detected a single cell, we defined the four equal area regions using the same angular span that was determined in the previous frames (during cytokinesis) of the same cell. Finally, we calculated the relative F-actin density in each region by

normalizing the total LifeAct signal to the area in each region. In cases where an adjacent, brighter cell was interfering with the cell of interest, we disregarded the signal in the affected region. Finally, we aligned the timing of different cells using the first frame where two separate cells were apparent (mid-anaphase).

Data presentation. To characterize the system noise, we repeatedly measured the node deviation of the same 12-µm-diameter polystyrene bead, size-normalized to SNACS and calculated the s.d. (Supplementary Fig. 6a). SNACS values of L1210 cells ($n = 24$ cells) were aligned to the latest time point where the cells maintained round morphology (3.8 min after anaphase onset; Fig. 3c,d). Then, we interpolated each data point for 0.01 h and calculated the mean value and s.d. of the interpolated data for each time point. All SNACS plots were filtered with a median filter of length 3, except in late mitosis (data points after anaphase onset), for which we show raw data. From the onset of anaphase, we calculated P values between the maximum and minimum within moving 5-min time blocks to characterize how much of the temporal change was statistically significant. We observed that temporal SNACS changes were not significant ($P > 0.05$, two-sided Welch's t-test) from 15.2 min after the onset of anaphase to cell division (Fig. 3, red dashed lines).

After defining the SNACS (Fig. 2), we illustrated all node-deviation changes, which reflect the mechanical property of a cell, by using SNACS or ΔSNACS. ΔSNACS represents the change in SNACS relative to the median value of the first 10–15 min of data presented (except in Fig. 4d, where the mean value of the whole cells before hypotonic shock is used), and was used only for better visualization of data.

Statistics and reproducibility. To quantify the agreement between the data from the experiments and the simulations (Fig. 1d–f), we calculated the coefficient of determination R^2. We assumed that the observed data were the experiments and the fitted were the simulations. Thus, for N data points where $y_{i,\text{experiment}}$ and $y_{i,\text{simulation}}$ are the observed and the fitted values ($i = 1, 2, \ldots, N$), we calculated

$$R^2 = 1 - \frac{\sum (y_{i,\text{experiment}} - y_{i,\text{simulation}})^2}{\sum (y_{i,\text{experiment}} - \bar{y})^2}, \text{where } \bar{y} = \frac{1}{N} \sum y_{i,\text{experiment}}$$

Statistical analyses were performed by Origin and MATLAB. We performed two-sided Welch's t-test for comparisons between two groups, and one-way ANOVA for comparisons between multiple groups. Post hoc analysis (Fisher's least significant difference) was performed only when ANOVA yielded a statistical difference ($P < 0.05$). The null hypothesis was always that mean values are the same. The detailed statistics performed for each experiment are described in figure legends.

All single-cell SNACS traces were obtained on separate days and were repeated at least five times in independent experiments. The population SNACS measurements were repeated in at least three independent experiments, and yielded comparable results.

FEM simulation. See Supplementary Note 2 for details.

Mass distribution correction. See Supplementary Note 3 and Supplementary Fig. 9 for details.

Orientation-dependent noise. See Supplementary Note 4 and Supplementary Fig. 15 for details.

Reduction of cortical thickness during swelling. See Supplementary Note 5 for details.

Reporting Summary. Further information on experimental design is available in the Nature Research Reporting Summary linked to this article.

Code availability

Code used in this study can be obtained from the corresponding author on reasonable request.

Data availability

The data that support the findings of this study are available from the corresponding author on reasonable request.

References

46. Lee, J. et al. Suspended microchannel resonators with piezoresistive sensors. *Lab Chip* **11**, 645–651 (2011).
47. Cetin, A. E. et al. Determining therapeutic susceptibility in multiple myeloma by single-cell mass accumulation. *Nat. Commun.* **8**, 1613 (2017).
48. Olcum, S., Cermak, N., Wasserman, S. C. & Manalis, S. R. High-speed multiple-mode mass-sensing resolves dynamic nanoscale mass distributions. *Nat. Commun.* **6**, 7070 (2015).
49. Dendukuri, D., Pregibon, D. C., Collins, J., Hatton, T. A. & Doyle, P. S. Continuous-flow lithography for high-throughput microparticle synthesis. *Nat. Mater.* **5**, 365–369 (2006).
50. Dendukuri, D., Gu, S. S., Pregibon, D. C., HattonT. A.. & Doyle, P. S. Stop-flow lithography in a microfluidic device. *Lab Chip* **7**, 818–828 (2007).
51. Hutter, J. L. & Bechhoefer, J. Calibration of atomic-force microscope tips. *Rev. Sci. Instrum.* **64**, 1868 (1993).
52. Elbert, D. L. & Hubbell, J. A. Conjugate addition reactions combined with free-radical cross-linking for the design of materials for tissue engineering. *Biomacromolecules* **2**, 430–441 (2001).
53. Anseth, K. S., Bowman, C. N. & Brannon-Peppas, L. Mechanical properties of hydrogels and their experimental determination. *Biomaterials* **17**, 1647–1657 (1996).

nature research

Corresponding author(s): Scott R. Manalis

Reporting Summary

Nature Research wishes to improve the reproducibility of the work that we publish. This form provides structure for consistency and transparency in reporting. For further information on Nature Research policies, see Authors & Referees and the Editorial Policy Checklist.

Statistical parameters

When statistical analyses are reported, confirm that the following items are present in the relevant location (e.g. figure legend, table legend, main text, or Methods section).

n/a	Confirmed	
☐	☒	The exact sample size (*n*) for each experimental group/condition, given as a discrete number and unit of measurement
☐	☒	An indication of whether measurements were taken from distinct samples or whether the same sample was measured repeatedly
☐	☒	The statistical test(s) used AND whether they are one- or two-sided *Only common tests should be described solely by name; describe more complex techniques in the Methods section.*
☒	☐	A description of all covariates tested
☐	☒	A description of any assumptions or corrections, such as tests of normality and adjustment for multiple comparisons
☐	☒	A full description of the statistics including central tendency (e.g. means) or other basic estimates (e.g. regression coefficient) AND variation (e.g. standard deviation) or associated estimates of uncertainty (e.g. confidence intervals)
☐	☒	For null hypothesis testing, the test statistic (e.g. *F*, *t*, *r*) with confidence intervals, effect sizes, degrees of freedom and *P* value noted *Give P values as exact values whenever suitable.*
☒	☐	For Bayesian analysis, information on the choice of priors and Markov chain Monte Carlo settings
☒	☐	For hierarchical and complex designs, identification of the appropriate level for tests and full reporting of outcomes
☐	☒	Estimates of effect sizes (e.g. Cohen's *d*, Pearson's *r*), indicating how they were calculated
☐	☒	Clearly defined error bars *State explicitly what error bars represent (e.g. SD, SE, CI)*

Our web collection on statistics for biologists may be useful.

Software and code

Policy information about availability of computer code

Data collection	LABVIEW 2012 for data collection and COMSOL 4.3 for simulations.
Data analysis	MATLAB R 2014B for all SNACS analysis and statistical tests, Igor Pro 8 for AFM data analysis, OriginPro 8 SR0 for plotting and statistical tests, Image J 1.47v for image display, DeltaVision software SoftWorx for image deconvolution.

For manuscripts utilizing custom algorithms or software that are central to the research but not yet described in published literature, software must be made available to editors/reviewers upon request. We strongly encourage code deposition in a community repository (e.g. GitHub). See the Nature Research guidelines for submitting code & software for further information.

Data

Policy information about availability of data

All manuscripts must include a data availability statement. This statement should provide the following information, where applicable:

- Accession codes, unique identifiers, or web links for publicly available datasets
- A list of figures that have associated raw data
- A description of any restrictions on data availability

The data that support the findings of this study are available from the authors on reasonable request.

Field-specific reporting

Please select the best fit for your research. If you are not sure, read the appropriate sections before making your selection.

☒ Life sciences ☐ Behavioural & social sciences ☐ Ecological, evolutionary & environmental sciences

For a reference copy of the document with all sections, see nature.com/authors/policies/ReportingSummary-flat.pdf

Life sciences study design

All studies must disclose on these points even when the disclosure is negative.

Sample size	No statistical tests were used to determine the sample size. The sample size (n) for single-cell traces (Fig. 3 and Fig. 4) refers to the number of cells independently monitored. The sample size for population measurements (Fig. 2, Fig. 3b, and Fig. 4d) reflects the number of cells measured within 20-30 minutes with a throughput, typically around 1,000-1,500 cells/hour.
Data exclusions	Single-cell traces: no data exclusions. Population comparisons - Asymmetric peaks (differences between left node deviation and right node deviation is bigger than 3 times the standard deviation of the instrument noise OR anti-node peaks with different height that is bigger than 3 times the standard deviation of the instrument noise) were excluded. This data exclusion criteria mostly results in exclusion of particles with buoyant mass lower than that of live cells (e.g. cell debris, which would bias the data) or cell clumps. All data exclusion criteria are also detailed in the Methods section.
Replication	All attempts at replication were successful. All single-cell SNACS traces were obtained on separate days. All single-cell SNACS traces were repeated at least five times in independent experiments. The population SNACS measurements were repeated at least in three independent experiments, always yielding comparable results.
Randomization	We did not use any pre-selection criteria on which cells to measure SNACS (stiffness measurement). A population of cells was loaded in to the SMR device and the first cell to go through was trapped for single cell monitoring experiments. For population measurements the order of drug treatments/measurements was randomized.
Blinding	Drug treatments and the consequent measurements were carried out by a single researcher, so no blinding was applicable. For image analysis, separate researchers carried out the imaging and image analysis. The researcher carrying out the image analysis was not aware of our experimental hypothesis.

Reporting for specific materials, systems and methods

Materials & experimental systems

n/a	Involved in the study
☒	☐ Unique biological materials
☒	☐ Antibodies
☐	☒ Eukaryotic cell lines
☒	☐ Palaeontology
☒	☐ Animals and other organisms
☒	☐ Human research participants

Methods

n/a	Involved in the study
☒	☐ ChIP-seq
☒	☐ Flow cytometry
☒	☐ MRI-based neuroimaging

Eukaryotic cell lines

Policy information about cell lines

Cell line source(s)	L1210 and BaF3 cell lines were obtained from ATCC. S-Hela cell line was kindly provided by Dr. Kevin Elias (Brigham and Women's Hospital, Department of Obstetrics and Gynecology, Boston, MA 02115).
Authentication	L1210 and BaF3 cell lines were authenticated by ATCC. S-Hela was not authenticated.
Mycoplasma contamination	L1210 and BaF3: tested for mycoplasma regularly. No contaminations have been found. S-Hela: not tested.
Commonly misidentified lines (See ICLAC register)	No commonly misidentified cell lines were used.